Nanoscale

Plastic Recovery and Self-healing in Longitudinally Twinned SiGe Nanowires

Journal:	*Nanoscale*
Manuscript ID	NR-ART-03-2019-002073.R1
Article Type:	Paper
Date Submitted by the Author:	14-Apr-2019

Complete List of Authors:	Shikder, Md Ruhul Amin; University of Illinois at Chicago Ramasubramanian, Ajaykrishna; University of Illinois at Chicago Maksud, Mahjabin; University of Illinois at Chicago Yurkiv, Vitaliy; University of Illinois at Chicago, Mechanical and Industrial Engineering Yoo, J.; Los Alamos National Laboratory, Harris, Charles; Sandia National Laboratories; Center for Integrated Nanotechnologies Vasudevamurthy, Gokul; General Atomics Mashayek, Farzad; University of Illinois at Chicago, The Micro- and Nanofluidics Laboratory, Department of Mechanical and Industrial Subramanian, Arunkumar; University of Illinois at Chicago,

Nanoscale

ARTICLE

Plastic Recovery and Self-healing in Longitudinally Twinned SiGe Nanowires

Received 00th January 20xx,
Accepted 00th January 20xx

DOI: 10.1039/x0xx00000x

www.rsc.org/

Md Ruhul Amin Shikder,[a] Ajaykrishna Ramasubramanian,[a] Mahjabin Maksud,[a] Vitaliy Yurkiv,[a] Jinkyoung Yoo,[b] Charles T. Harris,[c] Gokul Vasudevamurthy,[d] Farzad Mashayek,*[a] Arunkumar Subramanian *[a]

This paper reports on plastic recovery and self-healing behavior in longitudinally-twinned and [112] orientated SiGe nanowire (NW) beams when they are subjected to large bending strains. The NW alloys are comprised of lamellar nanotwin platelet(s) sandwiched between two semi-cylindrical twins. The loading curves, which are acquired from atomic force microscope (AFM) based three-point bending tests, reveal the onset of plastic deformation at a characteristic stress threshold, followed by further straining of the NWs. This ductility is attributed to dislocation activity within the semi-cylindrical crystal portions of the NW, which are hypothesized to undergo a combination of elastic and plastic straining. On the other hand, the lamellar nanoplatelets undergo purely elastic stretching. During the unloading process, the release of internal elastic stresses enables dislocation backflow and escape at the surface. As a result, the dislocations are predominantly annihilated and the NW samples evidenced self-healing via plastic recovery even at ultra-large strains, which are estimated using finite-element models at 16.3% in one of the tested devices. Finite element analysis also establishes the independence of the observed nanomechanical behavior on the relative orientation of the load with respect to the nanoplatelet. This first observation of reversible plasticity in the SiGe material system, which is aided by a concurrent evolution of segmented elastic and plastic deformation within its grains during the loading process, presents an important new pathway for mechanical stabilization of technologically important group-IV semiconductor nanomaterials.

Introduction

Nanowires, which are combinatorially sourced from group IV semiconductor materials such as silicon and germanium, have demonstrated performance attributes of relevance for nanoelectronics,[1,2] photonics,[3] thermoelectrics,[4] neuronal devices,[5] and lithium battery electrode applications.[6] Compositional mixing of Si and Ge has been achieved within these nanowire systems through alloying[1,7] as well as heterostructuring[5,6,8] approaches. This strategy has been employed in these past reports to promote / tune application-specific performance metrics such as charge carrier mobility, band-gap, electrical spin manipulation, and ionic diffusivity.

The nanomechanical performance and stability of Si-Ge materials is an important consideration in their eventual insertion within next-generation technologies. In the case of pure-Si and pure-Ge NWs, past reports have identified brittle behavior under tensile as well as flexural loading conditions, and have extracted material elastic modulus as well as fracture strength data from these experiments.[9, 10] On the other hand, atomic-scale transmission electron microscopy studies have been employed by other groups to show room-temperature plasticity in Si NWs.[11,12] In addition, Ma *et al.* have reported on the effect of Ge fraction as well as NW surface structure on the Young's modulus and fracture strength values observed in single-crystalline, [111] $Si_{1-x}Ge_x$ NW alloys.[13] These in-situ scanning electron microscopy (SEM) based tensile stretching experiments revealed a linear (monotonic) reduction in Young's modulus and an increase in fracture strength / strain with an increase in Ge content. While group-IV semiconductor NWs are single-crystalline when grown along the [111] direction, they exhibit longitudinal twinning when the growth axis extends along the [112] direction. Gamalski et. al used environmental transmission electron microscopy (ETEM) to image the growth process of Au-catalyzed [112] orientated Ge NWs via vapor-liquid-solid (VLS) technique.[14] This report attributed a twin plane re-entrant growth mechanism for preferential crystal nucleation / growth at the twin site.

In this paper, we present nanomechanical experiments involving longitudinally-twinned, [112] SiGe NW alloys. These NWs are comprised of semi-cylindrical crystals, which are separated by longitudinally oriented, lamellar nanotwin platelets (Fig. 1(a)). These NWs have been subjected to mid-length, flexural loading in the doubly-clamped configuration using an atomic-force microscope (AFM). The AFM force-

[a] Department of Mechanical and Industrial Engineering, University of Illinois at Chicago, Chicago, IL 60607, USA. E-mail: sarun@uic.edu and maskayek@uic.edu.
[b] Center for Integrated Nanotechnologies, Los Alamos National Laboratory, Los Alamos, NM 87545, USA.
[c] Center for Integrated Nanotechnologies, Sandia National Laboratories, Albuquerque, NM 87185, USA.
[d] General Atomics Corporation, San Diego, CA.

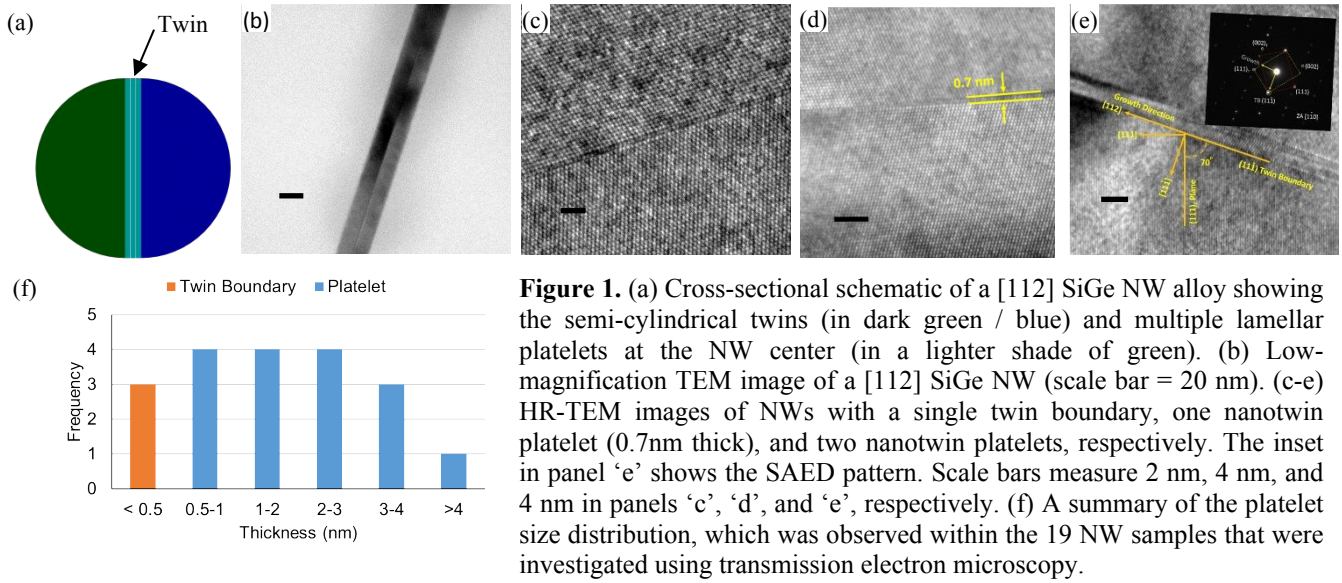

Figure 1. (a) Cross-sectional schematic of a [112] SiGe NW alloy showing the semi-cylindrical twins (in dark green / blue) and multiple lamellar platelets at the NW center (in a lighter shade of green). (b) Low-magnification TEM image of a [112] SiGe NW (scale bar = 20 nm). (c-e) HR-TEM images of NWs with a single twin boundary, one nanotwin platelet (0.7nm thick), and two nanotwin platelets, respectively. The inset in panel 'e' shows the SAED pattern. Scale bars measure 2 nm, 4 nm, and 4 nm in panels 'c', 'd', and 'e', respectively. (f) A summary of the platelet size distribution, which was observed within the 19 NW samples that were investigated using transmission electron microscopy.

deflection signatures and topographical images reveal plastic recovery and self-healing in these multi-crystalline NW systems, as opposed to the brittle behavior observed previously within the single-crystalline Si-Ge NW system.[13] This observation of plastic recovery is significant since it presents new pathways to engineer mechanical stability in these technologically important nanomaterial systems through microstructural engineering.

Material System, AFM Testing and Modeling Methodology

SiGe NW alloys, with a 50%-50% elemental composition and [112] growth direction, were synthesized using the vapor-liquid-solid growth technique. This growth of $Si_{0.5}Ge_{0.5}$ (or simply, SiGe) NWs was catalyzed by 30nm diameter Au nanoparticle seeds. The Au nanoparticles were first dispersed onto a Ge(111) substrate. The prepared substrate was then heated to up to 470°C under 3 Torr with hydrogen flow to form Au seeds. SiGe NWs were then synthesized by exposing the Au seeds to silane (SiH_4, 50%-diluted in H_2) and germane (GeH_4, 30%-diluted in H_2), which served as the precursors for the growth process. During the synthesis step, the chamber temperature and pressure were maintained at 425°C and 3 Torr, respectively. Transmission electron microscopy (TEM) imaging of as-grown NWs exhibited longitudinal twinning (Fig. 1). The samples for these microscopy experiments were obtained by adsorbing NWs on to a TEM grid by drop casting a NW suspension droplet on the surface of the grid and then, allowing it to air dry. TEM images revealed two semi-cylindrical, twinned crystals within the NWs. As shown in panels 'c' through 'e' of Fig. 1, the interface between these crystals is comprised of either a finite number of lamellar nanotwin platelets or a single twin boundary. It is important to note that an overwhelming majority or ~84% of the 19 NW samples, which were analyzed using the TEM, exhibited lamellar twin platelets while a much smaller number (i.e., the remaining 16% of the samples) exhibited a twin boundary interface between the semi-cylindrical crystals (Fig. 1(f)). This figure panel also lists the platelet thickness distribution, which was measured from the TEM micrographs using ImageJ software.

The SiGe NWs were extracted from the synthesized Ge(111) substrates and assembled as arrays of individual devices on silicon chips using dielectrophoresis (DEP). This assembly process has been detailed elsewhere and can be found in our past reports.[15-17] Briefly, the assembly substrates involved arrays of nanoelectrode pairs, which were deposited on an insulating silicon nitride surface and made of a metallization stack of 150nm-thick Au layer on top of a 5nm-thick Cr layer (for adhesion). The nanoelectrode pairs were defined using electron beam lithography, metal deposition, and metal lift-off steps. The DEP process starts with the suspension of NWs in ethanol, which is obtained through an ultrasonication of the NW containing growth substrate (i.e., Ge(111)) in ethanol. Next, an electric field map is imposed on the silicon chips by applying an AC bias between the nanoelectrode pairs. When NW suspension is pipetted on the silicon chip, the NWs experience DEP forces that yield their localization on the electrode gaps (i.e., the regions of field maxima). After the deposition is complete, the chip is dried with a nitrogen gun and the NWs adhere to the gold contacts via van der Waals interactions. Through suitable control of electric field strength, its frequency, NW concentration in the suspension, and deposition time, assembly of individual NWs is achieved. Finally, the assembled NWs are further anchored to gold electrode surfaces through electron-beam induced deposition (EBID) of Pt metal inside a FIB-SEM system. This process results in the creation of doubly-clamped, SiGe nanobeams, which are fully suspended in the region between the gold electrodes at their distal ends. Fig. 2 shows a schematic illustration and an atomic force micrograph of a representative SiGe nanowire device in panels 'a' and 'b', respectively.

Post assembly, the SiGe nanobeams were subjected to three-point bending tests using an AFM.[10, 18-21] In these experiments, the AFM tip is first positioned directly above the mid-length of the NW beam, under nanoscopic separation. Then, the sample stage is raised higher to first bring the NW in contact with the AFM tip and then, to deform the NW in the out-of-plane mode after establishment of contact. The AFM stage piezo movement (Z_{piezo}) and tip deflection (Z_{tip}) signals are recorded during this process. At each point during the post-contact stage of this experiment, the NW deflection (Z_{NW}) and AFM tip force (F_{tip}) can be calculated as:

$$Z_{\mathrm{NW}} = Z_{\mathrm{piezo}} - Z_{\mathrm{tip}} \quad (1)$$

and

$$F_{\mathrm{tip}} = k \cdot Z_{\mathrm{tip}} \quad (2)$$

In equation 2, the AFM tip stiffness (k) is calculated using Sader's method.[22] Thus, the Z_{tip} *vs.* Z_{piezo} data is transformed into an F_{tip} *vs.* Z_{NW} plot. This plot and the nanodevice topographical information (which is obtained from tapping mode AFM scans) are employed to analyze the response of SiGe NWs under nanomechanical loading. In these measurements, the post-contact travel range of the AFM z-piezo was on the order of ~50 to 140nm. This is determined by two factors: (i) the pre-set AFM ramp distance of 300nm, and (ii) the NW *vs.* tip separation distance prior to the loading experiment, which varies from one loading trial to the other and hence, results in the observed variation in the post-contact travel range. The rate at which the NW samples are subjected to mechanical loads can be controlled either through a choice of an AFM tip with a suitable mechanical stiffness or through a change in the duration of the loading-unloading cycle. In experiments presented in this report, the loading rate was varied through the use of AFM tips with different mechanical stiffness (which remained in the 1.2 N/m to 16.9 N/m range). The frequency of the loading-unloading cycles was maintained constant, at 1 Hz, across all trials. As discussed later, the longitudinally twinned NWs exhibit plastic deformation signatures upon loading beyond a characteristic threshold and recover this deformation upon removal of the AFM load.

An elasto-plastic, finite element (FE) model has been built using ANSYS software[23] in order to elucidate mechanisms underlying the experimentally observed relaxation and recovery behavior within the twinned SiGe NWs. The workflow employed to solve mechanics equations has been thoroughly described elsewhere[24] and a brief summary is as follows. The model considers the symmetrical characteristic of the fixed-end nanowire structure, as represented in the present AFM experiments, and the load from the tip is applied at the NW mid-length (Fig. 2(a)). In the AFM experiments, the NW is observed to undergo dynamic changes in its material properties during the loading-unloading cycle. This cycle is broadly divided into an initial elastic regime that terminates at a load drop, followed by another elastic-like straining regime and then, a plastic recovery regime during the retrace of the

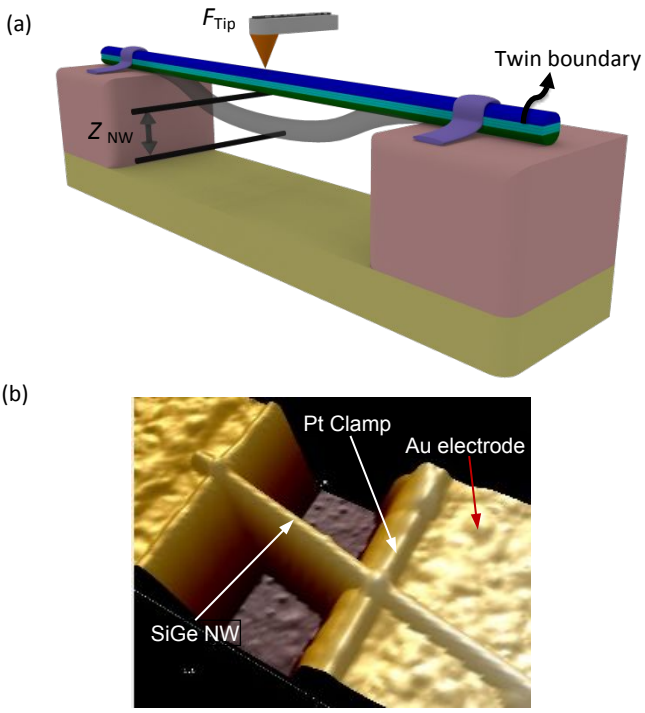

Figure 2. (a) Schematic illustration of the AFM three-point bending test, and (b) an AFM micrograph of a fabricated device (bottom). The image shows a single [112] SiGe NW beam, which is assembled in a doubly-clamped configuration across gold electrodes. The NW is anchored mechanically using top-side, EBID-defined Pt clamps.

AFM tip. This is captured in the model by a dynamic change in the Young's modulus (YM) of the semi-cylindrical crystals, while maintaining a constant YM for the nanotwin platelets. The assumption of YM changes only within the semi-cylindrical crystals is further explained in the following results section, where we hypothesize dislocation-free bond stretching (i.e., elastic deformation) within the nanotwin platelets, while the semi-cylindrical crystals experience dislocation activity and material modulation after the load drop. In the FE model, the NWs are discretized by employing tetrahedral elements. This element type is well suited for the cylinder shaped nanowire geometry and this element has plasticity, stress stiffening, large deflection, and large strain capabilities, which are required to fully capture the nanowire behavior during flexural loading. Also, geometric non-linearity is included to capture the effect of tension-induced stiffness on the bending deformations. Summation of the reaction forces calculated at the support points represents the force applied at the midpoint of the nanowire. Force and bending displacement variation is also monitored during unloading. Loading and unloading curves obtained from ANSYS simulations are compared against those obtained experimentally.

Results and Discussion

The F_{tip} *vs.* Z_{NW} plot for the NW device of Fig. 2 is shown in Fig. 3(a). As the NW is subjected to progressively increasing loads, it undergoes elastic deformation at tip forces below 204nN. Until this threshold, the NW deforms through a combination of flexural bending and tensile stretching, and exhibits a non-linear force-deflection relationship. At the yield load of 204 nN, which corresponds to a NW deflection of 49 nm, a sharp load drop is observed. Beyond the load-drop, the NW undergoes further straining up to a deformation of 119 nm. In the unloading curve, the load reduces to zero at a residual NW deformation of 85 nm, which represents the permanent set in conventional, non-recoverable beams. However, we find that this NW beam recovers its plastic deformation during the unloading process and returns to nearly overlap its initial elastic F_{tip} *vs.* Z_{NW} relationship at a 10 nm deflection.

We attribute the sharp drop in the loading curve to the onset of yielding in the NW via nucleation of dislocations at the surface of its semi-cylindrical crystals. Once nucleated, the dislocations glide swiftly with a very limited chance of interaction or multiplication and propagate to the center of the NW until they meet the twin boundary (TB), which acts as an interface barrier to their continued motion. As a result, subsequent dislocations pile up near the TBs, leading to an increased shear stress on the leading dislocation. Until this shear stress exceeds the TB barrier strength, the leading dislocation is not transmitted across the TB thereby, suppressing its fracture. In this regime that occurs beyond the load drop, the NW undergoes simultaneous straining in the elastic and plastic modes. While plastic straining is limited to the semi-cylindrical crystals, elastic straining may occur within both, the semi-cylindrical crystals as well as within the nanotwin platelets. The nanotwin lamellae have an average width of ~3 nm (calculated from the platelet size distribution observed within the 19 NW samples of Fig. 1(f)), which is too small to support plastic deformation and this hypothesis of dislocation-free bond-stretching is also supported by a past report involving in-situ TEM bending tests with Ni NWs.[25] These NWs contained ultra-thin lamellar twins of the type observed in our samples, and exhibited large and recoverable elastic strains within the lamellae at up to 34.6%. Furthermore, our argument related to the simultaneous deformation of the semi-cylindrical crystals through elastic and plastic straining is supported by the ex-situ TEM data presented for GaAs NWs after being subjected to bending tests.[26] In this report, the total NW strain was estimated using geometric shape factors, while the elastic strain was calculated through lattice distortion estimates from {111} d-spacing measurements. The difference between the total and elastic strains revealed the plastic strain component, and this approach established the simultaneous occurrence of elastic and plastic straining within the semiconductor NW crystals (as opposed to pure plastic deformation beyond yielding).

During the retraction of the AFM tip, the NW unloading curve returns to nearly overlap its initial elastic F_{tip} *vs.* Z_{NW} relationship at a deformation of 10nm. This indicates self-healing of the NW via plastic recovery and is further confirmed with topographical scans of the NW after the completion of the unloading process. This is evident from the AFM tip height plot acquired at the NW mid-length, which is shown before and after AFM testing in Fig. 4(a), and from the cross-sectional view of the suspended NW, which is shown in Fig. 4(d). We attribute the recovery of NW deformation to the predominant annihilation of dislocations within the semi-cylindrical crystals, which occurs through their backflow and eventual escape at the surface during the unloading process. This backflow mechanism is aided by the release of internal elastic stresses from both, the semi-cylindrical crystals as well as from the lamellar nanotwin segments of the NW. Reversible plasticity through release of internal stresses has been observed within multiple previous reports involving recovery of dislocation

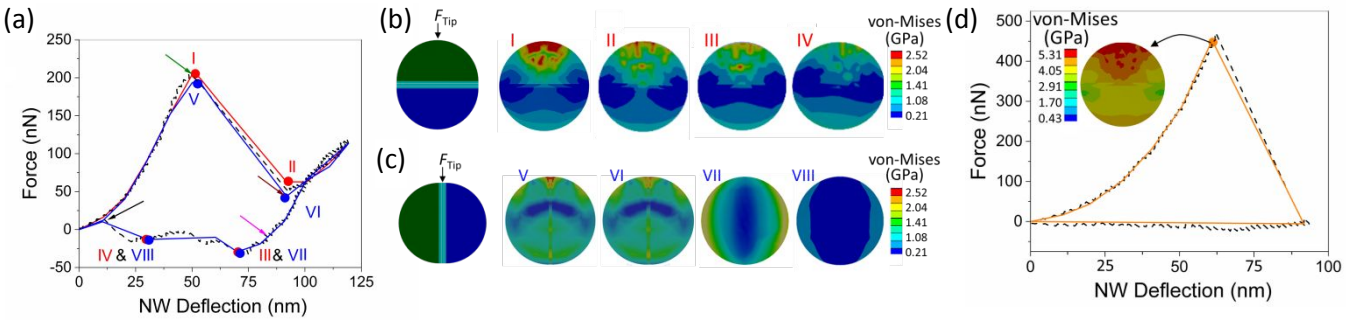

Figure 3. (a) A comparison between the F_{tip} *vs.* Z_{NW} curves obtained from the three-point bending test and from the finite-element model. The experimental data is presented with a black dashed line, while the blue and red solid lines represent models assuming a nanotwin platelet that is oriented perpendicular and parallel to the loading directions, respectively. There is a sharp load drop at a NW deflection of 49 nm (pointed with a green arrow), followed by an elastic-like regime up to a NW deformation of 119 nm (pointed with a brown arrow). In the retrace curve, the load drops to zero at a deformation of 85 nm (pointed with a purple arrow). However, this NW beam recovers its plastic deformation and returns to nearly overlap the loading curve at a 10 nm deflection (pointed with a black arrow) in the retrace curve. (b-c) The evolution of cross-sectional von–Mises stress contours, which develop at the mid-length of the NW during its loading and unloading cycles. Panels 'b' and 'c' represent cases where the load is applied perpendicular and parallel to the nanotwin platelet, respectively. For each of these two loading conditions, the stress contours are plotted at four different points on the F_{tip} *vs.* Z_{NW} curve: the onset of load drop (labelled I and V, which are also noted in the F_{tip} *vs.* Z_{NW} curve of panel 'a'), and the three distinct transition points for YM changes within the semi-cylindrical crystals (labelled II through IV, and VI through VIII). (d) The experimental (black dotted) and simulated (orange, blue) F_{tip} *vs.* Z_{NW} curves corresponding to a higher loading rate experiment (320 nN/sec here *vs.* 120 nN/sec for the data of panel 'a') that yielded fracture of the NW.

mediated as well as microstructural reconfiguration-enabled plasticity in both, metallic and non-metallic nanostructured materials. For instance, the orders of magnitude reduction in dislocation density observed after the unloading of GaAs NW crystals has been explained using the release of inhomogenous internal stresses.[26] Furthermore, reversible plasticity in polycrystalline gold and aluminum thin films has also been attributed to stress inhomogeneity and elastic stresses released from smaller grains.[27] On the other hand, we had recently reported on plastic recovery within polytypic, tunnel structured manganese dioxide NWs where release of elastic stresses within smaller width grains was hypothesized to aid in the reversibility of shear distortion-induced inter-layer reconfiguration within larger-width grains.[18] In the case of single crystalline, bcc metallic NWs such as Fe, Mo, and W, microstructural reconfiguration involving twinning induced yielding (under tensile loading) and its subsequent recovery via de-twinning (during the unloading process) has been identified as the underlying mechanism for superelasticity using molecular dynamics simulations.[28]

It is important to note that the assembly process does not yield control over the landing orientation of the NW TBs on top of the gold nanoelectrodes. Hence, the role of TB orientation (i.e., with respect to the AFM loading direction) on the NW mechanical properties and on its elasto-plastic deformation behavior was investigated using a FE model, which was built using the ANSYS software package (as noted in the previous section). In this model, the NW length, diameter, and nanotwin platelet width were set at 730 nm, 33 nm, and 3 nm, respectively. The NW length was estimated from SEM imaging (using ImageJ software), while its diameter was extracted from the AFM tip height plot of the NW in the region where it is located on top of the gold electrode. The 3 nm platelet width represents an averaged value based on the width distribution across 19 representative samples, which were discussed in the TEM data of Fig. 1(f). When the AFM load is perpendicular to the nanotwin platelet, FE curve-fitting to the experimental F_{tip} *vs.* Z_{NW} data revealed a NW YM of 50.8 GPa up to occurrence of the load drop (solid blue plot of Fig. 3(a)). Post-yielding, the YM of the semi-cylindrical crystals was modulated to fit the experimental data while keeping the YM of the nanotwin platelet constant. The change in the YM values of the semi-cylindrical crystals was determined by fitting it to the experimental data. This yielded a YM of 52 GPa, 51.2 GPa, and

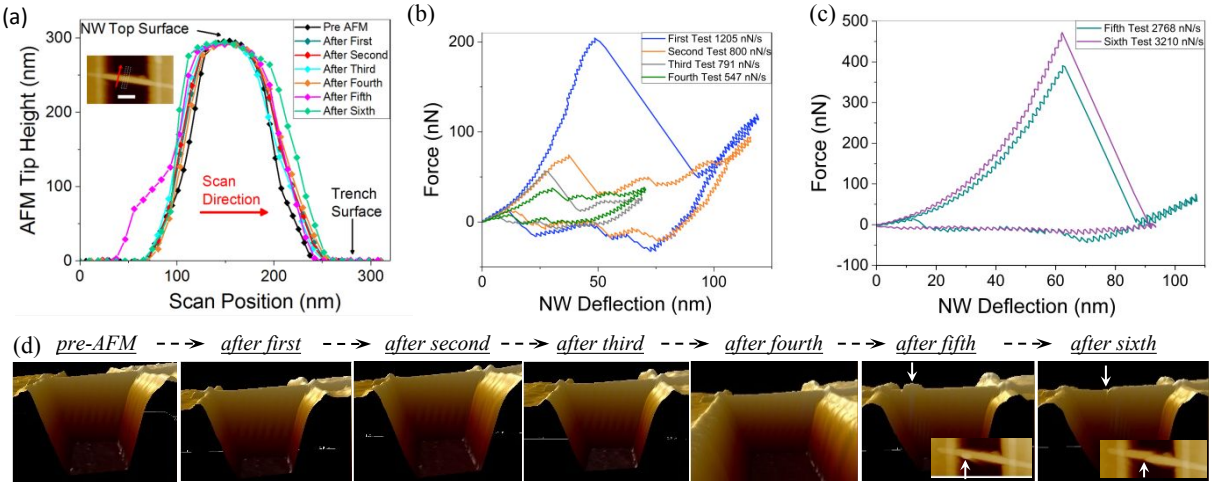

Figure 4. (a) Plots of the NW tip-height at its mid-length (i.e., the mid-point of its suspended region) as a function of scan position, shown before and after each successive loading-unloading experiment. The plotted data is averaged along the width of a 100nm wide rectangular region, which is centered at the NW mid-length and is highlighted with a white-box in the AFM top-view image (inset, scale bar = 200nm). (b) The F-d curves acquired from four sequential three-point bending experiments involving the NW of Figure 2. The curves were acquired within a time gap of ~3-7 minutes from each other. The loading rate for these experiments is calculated as the average ramp rate for the force within the elastic regime and is indicated in the figure legend. The sequential reduction in NW stiffness and yield point can be seen here. (c) The F_{tip} *vs.* Z_{NW} curves from experiments 5 and 6, which were acquired at higher loading rates. While the fifth experiment exhibits plastic recovery in the NW beam, the sixth experiment results in a brittle fracture of the NW. (d) AFM micrographs showing the evolution of the NW profile during the progression of the six loading experiments. These images show that the NW exhibits full plastic recovery during the first five trials. The bump on the NW after the fifth experiment white arrow) is a particle adsorbed on its surface, perhaps through transfer from the AFM tip during image acquisition. This is further confirmed by a particle attached to only one-side of the NW, as can be clearly seen in the top-view representation, which is provided in the inset. The micrograph obtained after the sixth loading trial highlights the fracture location with an arrow. The corresponding top-view of this micrograph is also shown in the inset.

50.8 GPa for the semi-cylindrical crystals in the regions between points II-III, III-IV, and after point IV of the F_{tip} *vs.* Z_{NW} curve, respectively (definition of labels I through IV are shown in Fig. 3(a)). Next, the NW force *vs.* deflection curve was simulated for the case when the nanotwin platelet is oriented parallel to the AFM load, while keeping the NW YM values the same as those obtained in case when the platelet was perpendicular to the loading direction. This result is shown using the solid red plot of Fig. 3(a) and it is evident that the force *vs.* deflection behavior remains nearly invariant, irrespective of the relative orientation between the platelet and the load.

In addition, the FE models confirm the development of nearly the same yield stresses on the surface of the semi-cylindrical crystals for both nanotwin platelet orientations and thereby, support the hypothesis of dislocation nucleation at the surface of these crystals at a characteristic material yield strength. The evolution of cross-sectional von Mises stress contours at the NW mid-length is shown at different points of the loading curve for the two platelet orientations in Fig. 3(b-c). When the load is perpendicular to the nanotwin platelet, the yield stress (which corresponds to the force at the onset of load-drop, or label 'I' in panel 'a') and the yield strain at the semi-cylindrical crystal surface were obtained as 2.52 GPa and 4.95%, respectively. The corresponding yield stress and yield strain for the parallel loading condition were obtained as 2.49 GPa and 4.89%, respectively. Thus, the FE modeling data of Fig. 3(a-c) confirms that for a given NW material (i.e., for a given YM and yield strength), its response to flexural loading is independent of the direction in which the mechanical load is applied. Furthermore, the peak strain, which is exerted at the end of the loading cycle at a NW deformation of 119nm, is estimated from the finite-element models as 16.3% (for both loading directions). This value for the recoverable strain is substantially higher than the 0.5% elastic strain limit observed with crystalline and ceramic materials at the bulk level.[29] It is also higher than the ~6% and ~12% recoverable strains (elastic + plastic) reported in Ref. 26 and Ref. 30, respectively, for GaAs NWs.

The repeatability of this plastic recovery behavior was further tested by subjecting the NW beam of Fig. 2 to additional AFM loading-unloading tests. These results are summarized in the F_{tip} *vs.* Z_{NW} plots of Fig. 4(b). In each of these experiments, the NW was tested with the same AFM tip (having a stiffness of 3.7 N/m) and at the same AFM tip ramp-rate of 1 Hz (i.e., the AFM sample stage is raised and lowered at the same rate to accomplish the loading-unloading process). We find that the NW experienced a sharp load-drop followed by further straining at increasing forces during each loading curve. Also, in each of these experiments, the NW exhibited plastic recovery at the later stages of the unloading process. The plastic recovery is further confirmed from the unchanged NW height scans (Fig. 4(a)), acquired at its mid-length, and from the cross-sectional image of the suspended NW (Fig. 4(d)). While load drops and reversible plasticity are common to each of the four experiments with this tip, the force-deflection curves reveal a progressive reduction in the stiffness and / or yield strength of the NW. Furthermore, the F_{tip} *vs.* Z_{NW} plot shows increasing linearity with progressive AFM testing cycles thereby, indicating a reduction in tensile stretching within the post-recovery NWs. We attribute these observations to the presence of residual dislocations within the shape recovered NW (post-unloading), though at a much lower density as compared to that just prior to unloading. This is similar to the observations reported in the case of GaAs NWs, where an orders of magnitude reduction in dislocation density was observed in the post-recovery NW sample.[26] These GaAs were reported to be very fragile after being subjected to large elastic+plastic strains and were observed to fracture upon exposure to even minor turbulence such as the gas flow inside the FIB-SEM microscope. This observation of fragility, presumably due to the presence of residual dislocations (though at a much reduced density), is consistent with the signature of reducing stiffness / strength evidenced in our NW device.

The dependence of this self-healing behavior on the loading rate was tested by subjecting the same NW device to a loading-unloading experiment using an AFM tip with a substantially higher stiffness AFM tip of 16.8 N/m (Fig. 4(c)). This represents a more than four-fold increase in tip stiffness, as compared to the 3.7 N/m tip used with the first four loading experiments of Fig. 4(b). As seen in Fig. 4(b-c), the yield load increases substantially from 38 nN in the fourth AFM test to 388 nN in the fifth AFM test when the average loading rate increases from 547 nN/sec to 2768 nN/sec. Beyond this threshold, the load drops to a near-zero force (i.e., to 4 nN) prior to the onset of a further straining regime at increasing loads. During the unloading process, we observe the NW return to an elastic straining regime at a deformation of 12 nm. The large load-drop associated with a reduction in force to near-zero values points to the high loading-rate induced development of micro-cracks within the semi-cylindrical crystals of the NW, which are partial and do not propagate along the entire width of the NW (i.e., through the lamellar nanotwins). However, a return to elastic deformation in the unloading part of the experiment points to self-healing of these microcracks through atomistic diffusion-mediated re-formation of bonds at the crack interface. This is similar to the in-situ TEM observation of partial fracture and subsequent self-healing in single-crystalline GaAs NWs, where the fracture was confined to the GaAs crystal while its surface oxide layer remained intact during loading.[31] While the restoration of elastic energy stored within the oxide layer was hypothesized as the driving force for bringing the fractured interfaces in proximity in Ref. 31, the elastic restoration energy in our case is expected to have its origins within the lamellar nanotwins. The NW device was subjected to another loading test (i.e., the sixth overall) with the high stiffness tip and it was observed to undergo complete and non-recoverable fracture at this step. This was evident from both, the absence of a return to elastic regime within the unloading portion of the F_{tip} *vs.* Z_{NW} curve

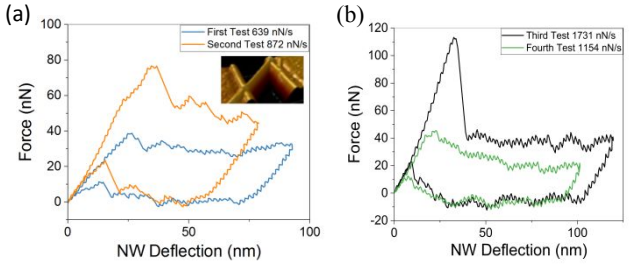

Figure 5. (a) The F_{tip} *vs.* Z_{NW} curve from the first two loading tests performed with a 3.7 N/m tip, with the AFM device image shown in the inset. (b) The F_{tip} *vs.* Z_{NW} curves acquired from the next two loading tests performed with a 16.8 N/m tip.

and from the AFM micrograph showing the fracture of the NW into two cantilevered segments (Fig. 4(c-d)). The data from this fracture event was also analyzed using our FE model, in order to extract the TB barrier strength of the NW device. The FE curve-fit to the experimental F_{tip} *vs.* Z_{NW} plot is shown in Fig. 3(c). The stress contours at the fracture point within this data were analyzed to determine a maximum stress of 5.22 GPa at the TB interface between the semi-cylindrical crystal and its adjoining nanotwin platelet (the corresponding value of strain is 10.3%). Thus, this stress value of 5.22 GPa represents the TB barrier strength, or the threshold for dislocation crossover beyond the TB. It is important to note that this TB barrier strength is more than twice the estimate for the NW yield strength (associated with dislocation nucleation) and further confirms our earlier arguments associated with ductility as well as recoverable plasticity confinement to the semi-cylindrical crystals when stresses do not exceed the TB barrier strength. Further insights into the dislocation-TB interactions may be obtained through atomistic simulations, such as the ones outlined in past reports involving nanotwinned Cu, Al, and Ni,[32, 33] and represents a future direction for further elucidating the dislocation-TB interaction mechanisms outlined in this effort.

This behavior of reversible plasticity was observed in a total of 20 AFM bending tests, which were performed on six different NW samples (the only additional test in these samples yielded fracture and was previously discussed in Fig. 4(c)). These experiments involved 14 instances where successive loading-unloading tests were performed on the same NW under identical experimental conditions i.e., the sample was pushed with the same AFM tip without changing its force ramp-rate. The remaining six involved instances where the tip was changed between experiments to either increase or decrease loading rates, such as the one involving the fourth and fifth bending tests on the NW device of Fig. 4. Out of the 14 instances when successive testing was performed on the same NW device using the same AFM tip, 11 instances resulted in discrete load drops in the preceding test followed by stiffness and / or yield load reduction in the subsequent one. On the other hand, in three instances involving loading rates below a 650 nN/sec threshold, the NW underwent substantial plastic deformation of at least several tens of nm at a near-constant or gradually reducing flow stress. This was followed by a stiffening of the NW in the subsequent loading-unloading cycle. One example of this behavior is shown in Fig. 5, where the first F_{tip} *vs.* Z_{NW} plot involved a loading rate of 639 nN/sec. However, the second loading-unloading test, which was performed with the same tip, evidenced a substantive stiffening of the NW. We attribute this behavior to increased dislocation-mediated plasticity and a high density of dislocation pile-up / entanglement in the first test due to its lower loading rate. This, in turn, results in an increase in the NW stiffness during the second loading-unloading cycle. It is important to note that a confirmation of this hypothesis requires further experimentation using new platforms that offer real-time microstructural imaging as well as simultaneous force-displacement measurements on the NW samples, which remains beyond the characterization capabilities of our testing platform / tool and those of other past ones involving plastic recovery in nanostructured materials.[11, 25-27, 30]

Conclusions

This effort has revealed a new nanomechanical performance regime involving plastic recovery and self-healing in SiGe NW alloys. Unlike brittle fracture observed within previous reports on single-crystalline, [111] orientated SiGe counterparts, these [112] NW beams contain twinned crystals and exhibit ductile behavior even when subjected to ultra-large strains, followed by deformation recovery and self-healing during removal of the externally exerted AFM load. This is attributed to the confinement of dislocation-mediated plasticity to NW segments that are comprised of semi-cylindrical twins. While the semi-cylindrical twins undergo a combination of elastic and plastic straining, the NW segment containing lamellar platelets undergoes pure elastic stretching. The release of this internally stored elastic energy is hypothesized to drive the plastic recovery mechanism via dislocation backflow. The results outlined in this paper establish the following new findings: (*i*) an avenue for engineering plasticity and its spontaneous self-reversibility (upon unloading) within nanostructured group IV semiconductors and beyond, and (*ii*) a direct measurement of the associated force-deflection signatures using an AFM and a subsequent quantification of critical material stresses / strains using finite element models, which is complimentary to the microstructural information that has been the predominant focus of past reports involving in-situ TEM based nanomechanical testing of reversible plasticity in nanomaterial systems.

Conflicts of interest

There are no conflicts to declare.

Acknowledgements

This work was partly supported by the National Science Foundation under Grant No. 1661038. Use of the Center for Nanoscale Materials, an Office of Science user facility, was supported by the U.S. Department of Energy, Office of Science, Office of Basic Energy Sciences, under Contract No. DE-AC02-06CH11357. The authors would specifically like to thank Dr. Ralu Divan, Ms. Suzanne Miller, and Dr. Dafei Jin for the technical support and training associated with the use of nanofabrication and characterization capabilities at the Center for Nanoscale Materials. This work was performed, in part, at the Sandia-Los Alamos Center for Integrated Nanotechnologies (CINT), a U.S. Department of Energy, Office of Basic Energy Sciences user facility under the user proposal C2015B0042. Sandia National Laboratories is a multimission laboratory managed and operated by National Technology and Engineering Solutions of Sandia LLC, a wholly owned subsidiary of Honeywell International Inc. for the U.S. Department of Energy's National Nuclear Security Administration under contract DE-NA0003525. This paper describes objective technical results and analysis. Any subjective views or opinions that might be expressed in the paper do not necessarily represent the views of the U.S. Department of Energy or the United States Government.

References

1 C. J. Delker, J. Y. Yoo, E. Bussmann, B. S. Swartzentruber and C. T. Harris, *Nanotechnology*, 2017, **28**, 46LT01.
2 H. K. Seong, E. K. Jeon, M. H. Kim, H. Oh, J. O. Lee, J. J. Kim and H. J. Choi, *Nano Lett.*, 2008, **8**, 3656–3661.
3 M. Amato, M. Palummo, R. Rurali and S. Ossicini, *Chem. Rev.*, 2013, **114**, 1371–1412.
4 M. Amato, S. Ossicini and R. Rurali, *Nano Lett.*, 2012, **12**, 2717–2721.
5 K. Y. Lee, S. Shim, I. S. Kim, H. Oh, S. Kim, J. P. Ahn, S. H. Park, H. Rhim and H. J. Choi, *Nanoscale Res. Lett.*, 2009, **5**, 410–415.
6 T. Song, H. Cheng, K. Town, H. Park, R. W. Black, S. Lee, W. I. Park, Y. Huang, J. A. Rogers, L. F. Nazar and U. Paik, *Adv. Func. Mater.*, 2013, **24**, 1458–1464.
7 S. G. Choi, P. Manandhar and S. T. Picraux, *J. Appl. Phys.*, 2015, **118**, 014303.
8 W. Lu, J. Xiang, B. P. Timko, Y. Wu and C. M. Lieber, *P. Natl. Acad. Sci.*, 2005, **102**, 10046–10051.
9 X. Wu, J. S. Kulkarni, G. Collins, N. Petkov, Almécija Dorothee, J. J. Boland, D. Erts and J. D. Holmes, *Chem. Mater.*, 2008, **20**, 5954–5967.
10 M. Maksud, J. Yoo, C. T. Harris, N. K. R. Palapati and A. Subramanian, *APL Mater.*, 2015, **3**, 116101.
11 L. Wang, K. Zheng, Z. Zhang and X. Han, *Nano Lett.*, 2011, **11**, 2382–2385.
12 K. Zheng, X. Han, L. Wang, Y. Zhang, Y. Yue, Y. Qin, X. Zhang and Z. Zhang, *Nano Lett.*, 2009, **9**, 2471–2476.
13 J. W. Ma, W. J. Lee, J. M. Bae, K. S. Jeong, Y. S. Kang, M.-H. Cho, J. H. Seo, J. P. Ahn, K. B. Chung and J. Y. Song, *Nano Lett.*, 2013, **13**, 1118–1125.
14 A. D. Gamalski, P. W. Voorhees, C. Ducati, R. Sharma and S.Hofmann, *Nano Lett.*, 2014, **14**, 1288–1292.
15 N. K. R. Palapati, E. Pomerantseva and A. Subramanian, *Nanoscale*, 2015, **7**, 3109–3116.
16 A. Subramanian, N. S. Hudak, J. Y. Huang, Y. Zhan, J. Lou and J. P. Sullivan, *Nanotechnology*, 2014, **25**, 265402.
17 S. K. Singh, N. Aryaan, M. R. A. Shikder, B. W. Byles, E. Pomerantseva and A. Subramanian, *Nanotechnology*, 2018, **30**, 025301.
18 M. R. A. Shikder, M. Maksud, G. Vasudevamurthy, B. W. Byles, D. A. Cullen, K. L. More, E. Pomerantseva and A. Subramanian, *Nanoscale Adv.*, 2019, **1**, 357-366.
19 M. Maksud, N. K. R. Palapati, B. W. Byles, E. Pomerantseva, Y. Liu and A. Subramanian, *Nanoscale*, 2015, **7**, 17642–17648.
20 L. T. Ngo, D. Alm´ecija, J. E. Sader, B. Daly, N. Petkov, J. D. Holmes, D. Erts and J. J. Boland, *Nano Lett.*, 2006, **6**, 2964–2968.
21 A. Heidelberg, L. T. Ngo, B. Wu, M. A. Phillips, S. Sharma, T. I. Kamins, J. E. Sader and J. J. Boland, *Nano Lett.*, 2006, **6**, 1101–1106.
22 B. Wen, J. E. Sader and J. J. Boland, *Phys. Rev. Lett.*, 2008, **101**, 175502.
23 ANSYS, Inc., ANSYS Mechanical Documentation v18.1. Canonsburg, PA, USA, 2018. http://www.ansys.com
24 P. Zhou, C. Wu and X. Li, *Meas. Sci. Technol.*, 2008, **19**, 115703.
25 L. Wang, P. Liu, P. Guan, M. Yang, J. Sun, Y. Cheng, A. Hirata, Z. Zhang, E. Ma, M. Chen and X. Han, *Nat. Comm.*, 2013, **4**, 2413.
26 P. Bao, Y. Wang, X. Cui, Q. Gao, H.-W. Yen, H. Liu, W. K. Yeoh, X. Liao, S. Du, H. H. Tan, C. Jagadish, J. Zou, S. P. Ringer and R. Zheng, *Appl. Phys. Lett.*, 2014, **104**, 021904.
27 J. Rajagopalan, J. H. Han and M. T. A. Saif, *Science*, 2007, **315**, 1831–1834.
28 S. Li, X. Ding, J. Deng, T. Lookman, J. Li, X. Ren, J. Sun and A. Saxena, *Phys. Rev. B*, 2010, **82**, 205435.
29 W. D. Callister, Jr. , Materials Science and Engineering An introduction, John Wiley & Sons, Inc. , New York2007.
30 Y.-B. Wang, L.-F. Wang, H. J. Joyce, Q. Gao, X.-Z. Liao, Y.-W. Mai, H. H. Tan, J. Zou, S. P. Ringer, H.-J. Gao and C. Jagadish, Adv. Mater., 2011 , **23,** 1356–1360.
31 Y. Wang, H. J. Joyce, Q. Gao, X. Liao, H. H. Tan, J. Zou, S. P. Ringer, Z. Shan and C. Jagadish, *Nano Lett.*, 2011, **11**, 1546–1549.
32 T. Zhu, J. Li, A. Samanta, H. G. Kim and S. Suresh, *P. Natl. Acad. Sci.*, 2007, **104**, 3031–3036.
33 Z.-H. Jin, P. Gumbsch, K. Albe, E. Ma, K. Lu, H. Gleiter and H. Hahn, *Acta Mater.*, 2008, **56**, 1126–1135.

Graphical Abstract

This article presents self-healing and mechanical stabilization in longitudinally-twinned SiGe nanowires through segmented elastic and plastic deformation within their grains.